

Distinct topological Hall responses in CeCu₂-type EuZn₂ and EuCd₂ films

Yuto Watanabe,¹ Shinichi Nishihaya,¹ Markus Kriener,² Ayano Nakamura,¹ and Masaki Uchida^{1, a)}

¹⁾*Department of Physics, Tokyo Institute of Technology, Tokyo 152-8551, Japan*

²⁾*RIKEN Center for Emergent Matter Science (CEMS), Wako 351-0198, Japan*

Rare earth intermetallic compounds crystallized in AlB₂-type and its low-symmetry derivative CeCu₂-type structures potentially host diverse frustrated magnetic structures and rich magnetotransport phenomena. We report the film growth of CeCu₂-type EuZn₂ by molecular beam epitaxy and the observation of topological Hall responses highly contrastive to isostructural EuCd₂. While their magnetization curves are rather similar, the topological Hall effect observed in EuZn₂ is simpler, with the only one component enhanced at the magnetic transition field. EuZn₂ may be a unique system for studying the magnetic domain boundary effect on topological Hall responses among the CeCu₂-type rare-earth intermetallic compounds.

^{a)} Author to whom correspondence should be addressed: m.uchida@phys.titech.ac.jp

Transverse motion of carriers neither proportional to the magnetic field nor the magnetization has attracted broad interest both in fundamental and applied physics¹. Such a nonmonotonic Hall response originates in a change in the real-space or momentum-space Berry curvature in the magnetization process. In particular, the Hall response reflecting a real-space spin texture is termed topological Hall effect (THE), where a noncoplanar spin texture with finite scalar spin chirality, defined by the solid angle spanned by three adjacent spins, generates an emergent magnetic field on charged carriers^{2,3}. A magnetic skyrmion lattice is a typical example of the noncoplanar spin texture. Recently, the range of skyrmion host compounds has been expanded from noncentrosymmetric chiral to centrosymmetric frustrated magnets⁴⁻⁸.

As centrosymmetric magnets which can host a skyrmion lattice, AlB_2 -type compounds represented by Gd_2PdSi_3 have attracted growing attention⁷. For example in Gd_2PdSi_3 , a magnetic Gd triangular lattice layer and a Pd/Si honeycomb lattice layer are alternately stacked to form a two-dimensionally frustrated system, where a giant topological Hall response is observed with rather monotonic change in magnetization⁷. The AlB_2 -type structure is also famous for many lower-symmetry derivatives including the $CeCu_2$ -type one⁹. In rare-earth intermetallic compounds RA_2 ($R = La - Lu$, $A = Zn, Cd, \text{ or } Cu$) with the $CeCu_2$ -type structure, a distorted R triangular lattice layer and a three-dimensionally buckled A honeycomb lattice layer are alternately stacked¹⁰. Differences in distortion and buckling as well as magnetic anisotropy of rare-earth magnetic moments can bring about diverse frustrated magnetic structures and magnetotransport in RA_2 . In addition to helical magnetic ordering with various propagation directions and rotation planes as observed in $GdCu_2$ and $PrZn_2$ ^{14,17,22}, rich topological Hall responses have been recently found for $EuCd_2$ ³⁰. However, comprehensive research on the magnetotransport in RA_2 is still lacking.

Figure 1(a) summarizes the ratio of out-of-plane and in-plane rare-earth atomic distances (d_{out} and d_{in}) in $CeCu_2$ -type intermetallic compounds^{11-21,23-29}. In most of them including $EuCd_2$, pairs of the nearest neighbor rare-earth atoms are formed between the adjacent triangular lattice layers ($d_{out} < d_{in}$). Actually, $EuZn_2$ is the only magnetic compound with such pairs within the triangular lattice layers ($d_{out} > d_{in}$), since $LaZn_2$ is nonmagnetic. Drastic changes in magnetotransport can be thus expected reflecting the different frustration arrangements of the Eu^{2+} isotropic magnetic moments^{11,12}, as compared in Figs. 1(b) and 1(c). In this paper, we report film growth of $EuZn_2$ by molecular beam epitaxy and

observation of topological Hall responses highly contrastive to EuCd_2 .

Thin films of EuZn_2 and EuCd_2 were grown on Al_2O_3 (0001) substrates using an Epiquest RC1100 II-V molecular beam epitaxy chamber^{30–35}. The growth temperature for EuZn_2 films was typically set to 400 °C. Eu and Zn were supplied by an effusion cell with a Zn-rich flux ratio ($P_{\text{Zn}}/P_{\text{Eu}} = 6$). This flux ratio is lower than in the growth of EuCd_2 films ($P_{\text{Cd}}/P_{\text{Eu}} = 15 - 44$)³⁰, consistent with the less volatile nature of Zn compared to Cd. The film thickness is designed at 65 nm. As confirmed in Figs. 2(a) and 2(b), x-ray diffraction 2θ - ω scans for both EuZn_2 and EuCd_2 films exhibit sharp peaks from the (020) lattice plane without any impurity peaks, indicating that the distorted Eu triangular lattice layers are stacked on the Al_2O_3 (0001) plane.

Figures 2(c) – 2(f) compare fundamental magnetic properties taken for EuZn_2 and EuCd_2 films. The temperature dependence of the magnetization M exhibits a cusp at the Néel temperature $T_{\text{N}} = 35$ K for EuZn_2 and 37 K for EuCd_2 , almost consistent with previous reports in polycrystalline bulks^{11,12}. Both in the EuZn_2 and EuCd_2 films, M keeps increasing below T_{N} , suggesting that their magnetic ground states are not a simple collinear antiferromagnetic ordering. Magnetization curves, taken with sweeping the out-of-plane field B_{out} at 2 K, are rather monotonic and also quite similar between EuZn_2 and EuCd_2 . A transition from phase I to II occurs at the metamagnetic transition field $B_{\text{m}} = 2.3$ T for EuZn_2 and 1.3 T for EuCd_2 with tiny hysteresis, and then the Eu^{2+} magnetic moments are forcedly aligned along the out-of-plane direction above the saturation field $B_{\text{s}} = 5.1$ T for EuZn_2 and 3.8 T for EuCd_2 . Another small hysteresis loop is confirmed centered at 0 T, indicating that there is a weak ferromagnetic component at the ground state of EuZn_2 as well as EuCd_2 .

Figure 3 summarizes magnetotransport observed for the EuZn_2 film. As shown in Fig. 3(a), the temperature dependence of the longitudinal resistivity ρ_{xx} is metallic with a residual resistivity ratio (RRR) of 7. It exhibits a clear kink at T_{N} , reflecting strong coupling between the itinerant carriers and the localized Eu^{2+} magnetic moments. In the out-of-plane field dependence shown in Fig. 3(b), ρ_{xx} exhibits a peak at B_{m} and then negative magnetoresistance up to B_{s} . Figure 3(c) shows the Hall resistivity ρ_{yx} measured with sweeping the out-of-plane field B_{out} at 2 K. The hole density estimated by fitting the ρ_{yx} curve above the saturation field at 2 K is $1.7 \times 10^{22} \text{ cm}^{-3}$, which is similar to that of EuCd_2 ³⁰. It is clear that there is a nonmonotonic Hall component in addition to the ordinary Hall resistivity ρ_{yx}^{O} and the anomalous Hall resistivity ρ_{yx}^{A} . Here ρ_{yx}^{O} is expressed by $\rho_{yx}^{\text{O}} = R_0 B_{\text{out}}$ with the

Hall coefficient R_0 , and ρ_{yx}^A is extracted by $\rho_{yx}^A = r_s \rho_{xx}^2 M$ with r_s determined as a fitting parameter, since the longitudinal conductivity converted from ρ_{xx} is located in the so-called intrinsic region of the conventional scaling plot³⁶. Figure 3(d) displays the additional component obtained by subtracting ρ_{yx}^O and ρ_{yx}^A from the measured Hall resistivity. Hereafter we call this ρ_{yx}^T , which is ascribed to the topological Hall component originating in frustrated spin configuration, as discussed below.

ρ_{yx}^T appears below T_N , indicating that it is related to the magnetic ordering. As reported for some magnetic compounds, ρ_{yx} may be affected by the change in ρ_{xx} through a field dependence of the scattering time. In ErB₄, for example, a nonmonotonic Hall component has been explained by a modified two-band model incorporating this effect³⁷. In the present case, however, the fitting curve of $\rho_{yx}^O + \rho_{yx}^A$ swells rather in the direction opposite to the hump around 2.5 T, and thus the change in the scattering time would not be the cause.

Here comparison with EuCd₂ is helpful for discussion. Figures 4(a) and 4(b) compare ρ_{yx}^T taken for EuZn₂ and EuCd₂ at 2 K. In EuZn₂, only the peak P1 appears centered at B_s between phase I and II. In EuCd₂, on the other hand, ρ_{yx}^T is characterized by three peaks P1-P3, and among them, peak P1 similarly appears centered at B_s as in EuZn₂. Another difference is that a large hysteresis loop is observed in EuCd₂ accompanied with a sharp enhancement of P1 at low temperatures. The origin of THE in EuCd₂ has been understood the real-space spin Berry curvature, or noncoplanar spin textures realized on the distorted Eu^{2+} triangular lattice layers³⁰. It has been clarified based on the temperature dependence measurements that the sign of the THE peaks P1-P3 originating from the real-space spin Berry curvature remain unchanged, while ρ_{yx}^A reflecting the momentum-space Berry curvature exhibits a sign change at 20 K. Although the sign change of ρ_{yx}^A does not occur in EuZn₂ at elevated temperatures, it is reasonable to suggest that THE in EuZn₂ also originates in noncoplanar spin textures in the magnetization process, considering the similarity of the magnetization properties between the two materials. In fact, the distorted Eu triangular lattice in the ac -plane of CeCu₂-type structure can host uncanceled local Dzyaloshinskii-Moriya interaction which favors spin configuration canted from the ac -plane to the out-of-plane b -axis, possibly leading to a noncoplanar ordering.

Figures 4(c) and 4(d) compare a color-map of ρ_{yx}^T taken in the downward field sweep on the $B_{\text{out}}-T$ phase diagram. In EuZn₂, ρ_{yx}^T consisting only of the peak P1 appears anti-symmetric to the magnetic field and continues to reach a maximum value at the magnetic

transition field between phases I and II even upon increasing temperature. In EuCd_2 , the appearance of ρ_{yx}^T is more complex and not antisymmetric to the field due to the large hysteresis at low temperatures, but the enhancement of P1 at the magnetic transition field is commonly confirmed in the negative field region. As the peak P1 is enhanced not within a specific phase but at a phase boundary, it is naturally ascribed to the magnetic domain boundary formed between the two phases. In evidence, it has been demonstrated that P1 in EuCd_2 strongly depends on the field cooling processes, which can effectively modulate the domain boundary density³⁰. On the other hand, the differences in the appearance of THE between EuZn_2 and EuCd_2 are probably derived from different pairs of the nearest neighbor Eu atoms and dominant magnetic interactions as illustrated in Fig. 4(c). While spin modulation propagating along the c -axis has been reported for other intermetallic compounds $R\text{Zn}_2$ with $d_{\text{out}} < d_{\text{in}}$ ^{13,14,16,17}, distinctive magnetic structures are realized in EuZn_2 with $d_{\text{out}} > d_{\text{in}}$, which deserve clarification in future studies. The appearance of a simple single-component THE also suggests that EuZn_2 is potentially a unique system for further studying the magnetic domain boundary effect on THE among the CeCu_2 -type rare-earth intermetallic compounds.

In summary, we have grown EuZn_2 thin films by molecular beam epitaxy and revealed topological Hall responses which are in sharp contrast to EuCd_2 . While their magnetization curves in the magnetization process are rather similar, the topological Hall effect observed in EuZn_2 is simpler, with the only one component enhanced at the metamagnetic transition field. Hence, we propose EuZn_2 as a unique system for further studying the magnetic domain boundary effect on THE among the CeCu_2 -type rare-earth intermetallic compounds.

ACKNOWLEDGMENTS

We thank M. Kawasaki for help in a part of the magnetization measurements. We also thank H. Ishizuka, Y. Yamasaki, T. Nakajima, F. Kagawa, and K. Matsuura for fruitful discussions. This work was supported by JST FOREST Program Grant No. JPMJFR202N, Japan, by Grant-in-Aids for Scientific Research JP22H04471, JP22H04501, JP22K18967, JP22K20353, JP23K13666, JP24H01614, and JP24H01654 from MEXT, Japan, and by STAR Award funded by the Tokyo Tech Fund, Japan.

CONFLICT OF INTEREST

The authors have no conflicts to disclose.

AUTHOR CONTRIBUTIONS

Yuto Watanabe: Data curation (lead); Formal analysis (equal); Investigation (lead); Methodology (equal); Visualization (lead); Writing - original draft preparation (lead). **Shinichi Nishihaya:** Formal analysis (equal), Investigation (equal), Methodology (equal), Writing-review & editing (equal). **Markus Kriener:** Formal analysis (supporting), Investigation (equal), Writing - review & editing (equal). **Ayano Nakamura:** Formal analysis (supporting), Investigation (supporting), Writing - review & editing (equal). **Masaki Uchida:** Conceptualization (lead); Funding acquisition (lead); Methodology (lead); Project administration (lead); Supervision (lead); Writing - review & editing (lead).

DATA AVAILABILITY

The data that supports the findings of this study are available from the corresponding author upon reasonable request.

REFERENCES

- ¹N. Nagaosa, J. Sinova, S. Onoda, A. H. MacDonald, and N. P. Ong, *Rev. Mod. Phys.* **82**, 1539–1592 (2010).
- ²K. Ohgushi, S. Murakami, and N. Nagaosa, *Phys. Rev. B* **62**, R6065(R) (2000).
- ³Y. Taguchi, Y. Oohara, H. Yoshizawa, N. Nagaosa, and Y. Tokura, *Science* **291**, 2573-2576 (2001).
- ⁴S. Mühlbauer, B. Binz, F. Jonietz, C. Pfleiderer, A. Rosch, A. Neubauer, R. Georgii, and P. Böni, *Science* **323**, 915-919 (2009).
- ⁵N. Kanazawa, Y. Nii, X.-X. Zhang, A. S. Mishchenko, G. De Filippis, F. Kagawa, Y. Iwasa, N. Nagaosa, and Y. Tokura, *Nat. Commun.* **7**, 11622 (2016).
- ⁶X. Z. Yu, N. Kanazawa, Y. Onose, K. Kimoto, W. Z. Zhang, S. Ishiwata, Y. Matsui, and Y. Tokura, *Nat. Mater.* **10**, 106-109 (2011).

- ⁷T. Kurumaji, T. Nakajima, M. Hirschberger, A. Kikkawa, Y. Yamasaki, H. Sagayama, H. Nakao, Y. Taguchi, T. Arima, and Y. Tokura, *Science* **365**, 914-918 (2019).
- ⁸R. Takagi, N. Matsuyama, V. Ukleev, L. Yu, J. S. White, S. Francoual, J. R. L. Mardegan, S. Hayami, H. Saito, K. Kaneko, K. Ohishi, Y. Ōnuki, T. Arima, Y. Tokura, T. Nakajima, and S. Seki, *Nat. Commun.* **13**, 1472 (2022).
- ⁹R.-D. Hoffman and R. Pöttgen, *Z. Kristallogr.* **216**, 127-145 (2001).
- ¹⁰D. Debray, *J. Less-Common Met.* **30**, 237-248 (1973).
- ¹¹K. H. J. Buschow, and F. J. van Steenwijk, *Physica B* **85**, 122-126 (1977).
- ¹²K. H. J. Buschow, W. J. Huiskamp, H. Th LeFever, F. J. v Steenwijk, and R. C. Thiel, *J. Phys. F: Met. Phys.* **5**, 1625 (1975).
- ¹³D. Debray, M. Sougi, and P. Meriel, *J. Chem. Phys.* **56**, 4325-4328 (1972).
- ¹⁴M. Ohashi, T. Kitai, T. Kaneko, S. Abe, S. Funahashi, and Y. Yamaguchi, *J. Magn. Magn. Mater.* **140**, 1119-1120 (1995).
- ¹⁵G. Borzone, G. Cacciamani, R. Ferro, J. Charles, and J. Hertz, *J. Less-Common Met.* **128**, 297-312 (1987).
- ¹⁶D. Debray and M. Sougi, *J. Chem. Phys.* **58**, 1783-1786 (1972).
- ¹⁷M. Ohashi, T. Kitai, T. Kaneko, H. Yoshida, Y. Yamaguchi, and S. Abe, *J. Magn. Magn. Mater.* **90**, 585-586 (1990).
- ¹⁸D. Debray and M. Sougi, *J. Chem. Phys.* **57**, 2156-2189 (1972).
- ¹⁹D. J. Michel and E. Ryba, *J. Less-Common Met.* **18**, 159-165 (1969).
- ²⁰R. Trump, S. Thierfeldt, M. Loewenhaupt, and T. Chattopadhyay, *J. Appl. Phys.* **69**, 4699-4701 (1991).
- ²¹C. S. Garde, J. Ray, and G. Chandra *J. Phys.: Condens. Matter* **5**, 6737-6744 (1993).
- ²²M. Rotter, A. Lindbaum, E. Gratz, G. Hilscher, H. Sassik, H. E. Fischer, M. T. Fernandez-Diaz, R. Arons, and E. Seidl, *J. Mag. Mag. Mater.* **214**, 281-290 (2000).
- ²³Z. Kanghou, and H. Chunxiao, and C. Lili, *J. Alloys Compd.* **189**, L31-L33 (1992).
- ²⁴G. A. Costa and E. A. Franceschi, *J. Less-Common Met.* **106**, 175-182 (1985).
- ²⁵E. Franceschi, *J. Less-Common Met.* **87** 249-256 (1982).
- ²⁶Z. Smetana and V. Šíma, *J. Magn. Magn. Mater.* **59**, 145-152 (1986).
- ²⁷A. R. Storm and K. E. Benson, *Acta Cryst.* **16**, 701-702 (1963).
- ²⁸E. Gratz, A. Lindbaum, and M. Rotter, *J. Phys.: Condens. Matter* **5**, 7955-7958 (1993).
- ²⁹A. Iandelli and A. Palenzona, *J. Less-Common Met.* **25**, 333-335 (1971).

- ³⁰S. Nishihaya, Y. Watanabe, M. Kriener, A. Nakamura, and M. Uchida, *Phys. Rev. B* **110**, 035159 (2024).
- ³¹M. Uchida, S. Sato, H. Ishizuka, R. Kurihara, T. Nakajima, Y. Nakazawa, M. Ohno, M. Kriener, A. Miyake, K. Ohishi, T. Morikawa, M. S. Bahramy, T. Arima, M. Tokunaga, N. Nagaosa, and M. Kawasaki, *Sci. Adv.* **7**, eabl5381 (2021).
- ³²M. Ohno, S. Minami, Y. Nakazawa, S. Sato, M. Kriener, R. Arita, M. Kawasaki, and M. Uchida, *Phys. Rev. B* **105**, L201101 (2022).
- ³³S. Nishihaya, A. Nakamura, M. Ohno, M. Kriener, Y. Watanabe, M. Kawasaki, and M. Uchida, *Appl. Phys. Lett.* **124**, 023103 (2024).
- ³⁴M. Ohno, M. Uchida, Y. Nakazawa, S. Sato, M. Kriener, A. Miyake, M. Tokunaga, Y. Taguchi, and M. Kawasaki, *APL Mater.* **9**, 051107 (2021).
- ³⁵M. Ohno, M. Uchida, R. Kurihara, S. Minami, Y. Nakazawa, S. Sato, M. Kriener, M. Hirayama, A. Miyake, Y. Taguchi, R. Arita, M. Tokunaga, and M. Kawasaki, *Phys. Rev. B* **103**, 165144 (2021).
- ³⁶S. Onoda, N. Sugimoto, and N. Nagaosa, *Phys. Rev. B* **77**, 165103 (2008).
- ³⁷L. Ye, T. Suzuki, and J. G. Checkelsky, *Phys. Rev. B* **95**, 174405 (2017).

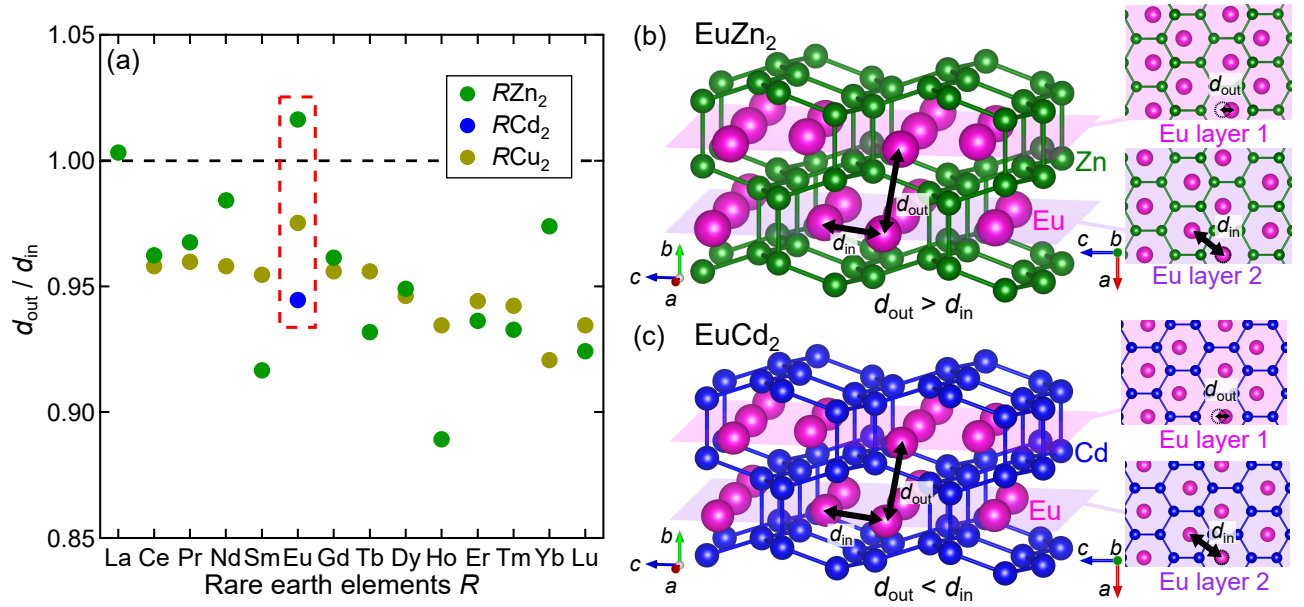


FIG. 1. Crystal structure and atomic distances of CeCu₂-type rare-earth intermetallic compounds. (a) Ratio of out-of-plane and in-plane rare-earth atomic distances (d_{out}/d_{in}) in CeCu₂-type RA_2 ($R = \text{La} - \text{Lu}$, $A = \text{Zn}$, Cd , or Cu)^{11–21,23–29}. Crystal structure of (b) EuZn₂ and (c) EuCd₂, composed of alternate stacking of a distorted Eu triangular lattice layer and a buckled Zn or Cd honeycomb lattice layer along the b -axis. While pairs of the nearest neighbor Eu atoms are formed within the triangular lattice layers in EuZn₂ ($d_{out} > d_{in}$), they are between the adjacent layers in EuCd₂ ($d_{out} < d_{in}$).

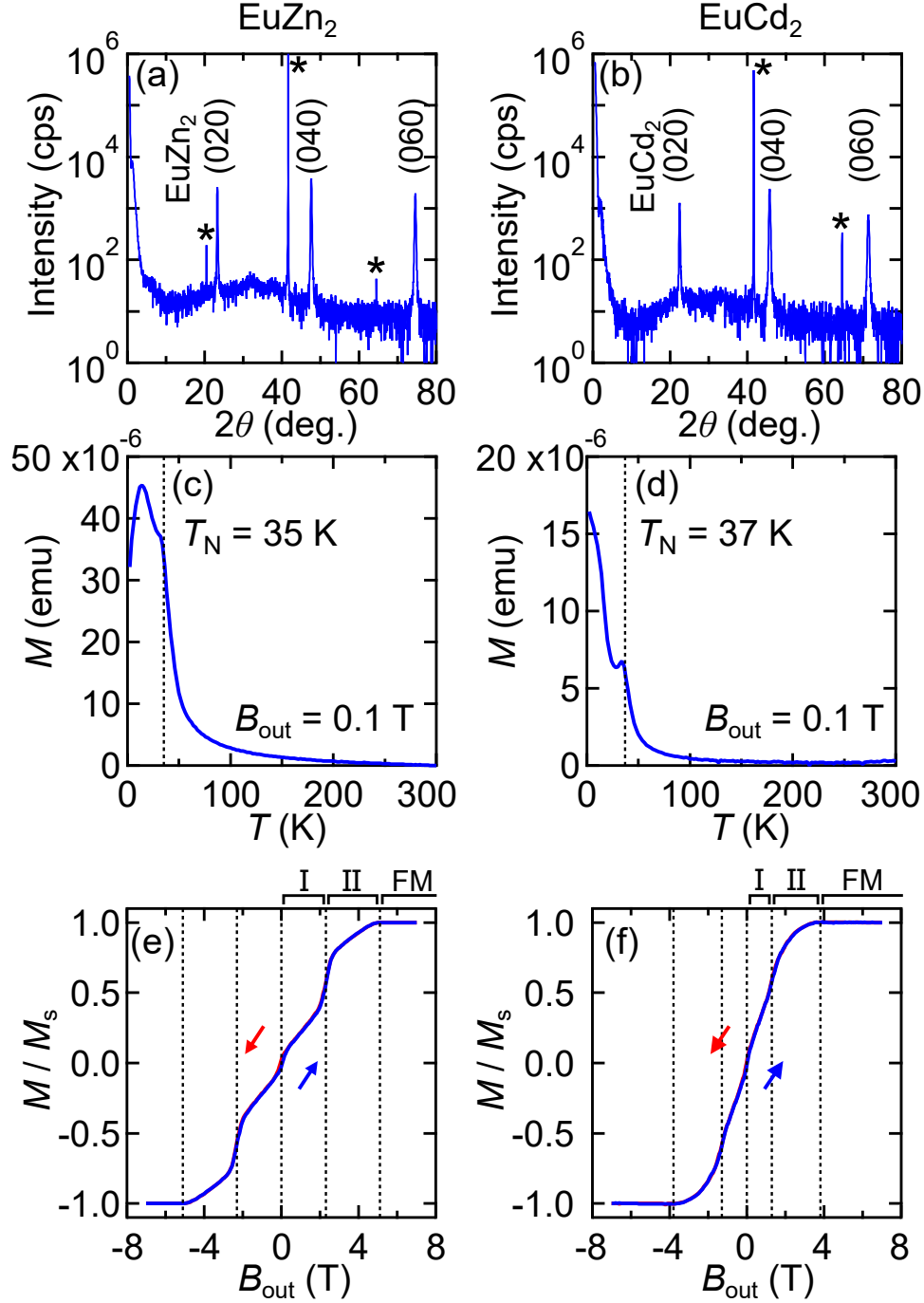


FIG. 2. Magnetic properties of EuZn_2 and EuCd_2 thin films. X-ray diffraction 2θ - ω scans of (010)-oriented (a) EuZn_2 and (b) EuCd_2 films grown on the Al_2O_3 (0001) substrate. An asterisk denotes the diffraction peaks from the Al_2O_3 substrate. Temperature dependence of the magnetization in (c) EuZn_2 and (d) EuCd_2 films, measured in an out-of-plane magnetic field of $B_{\text{out}} = 0.1$ T. Magnetization curves of (e) EuZn_2 and (f) EuCd_2 films taken with sweeping B_{out} at 2 K. Data are normalized by the saturation magnetization M_s .

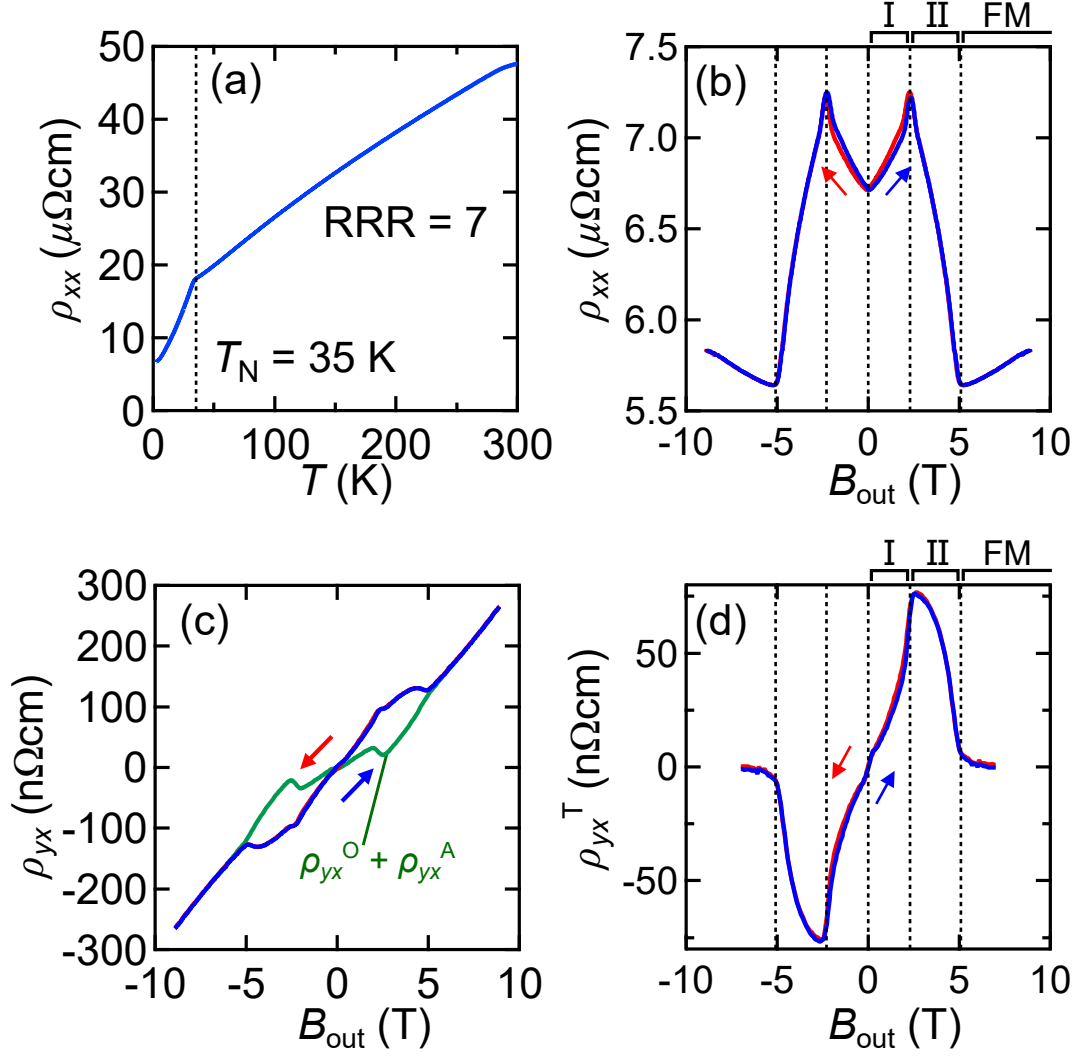


FIG. 3. Magnetotransport of the EuZn₂ film. (a) Temperature dependence of longitudinal resistivity ρ_{xx} . Out-of-plane field dependence of (b) ρ_{xx} and (c) Hall resistivity ρ_{yx} at 2 K. ρ_{yx} data above the saturation field is fitted by a green curve consisting of the ordinary Hall component ($\rho_{yx}^{\text{O}} = R_0 B_{\text{out}}$) and the anomalous Hall component ($\rho_{yx}^{\text{A}} = r_s \rho_{xx}^2 M$) with field-independent constants R_0 and r_s . (d) Topological Hall component ρ_{yx}^{T} at 2 K, obtained by subtracting $\rho_{yx}^{\text{O}} + \rho_{yx}^{\text{A}}$ from ρ_{yx} in (c).

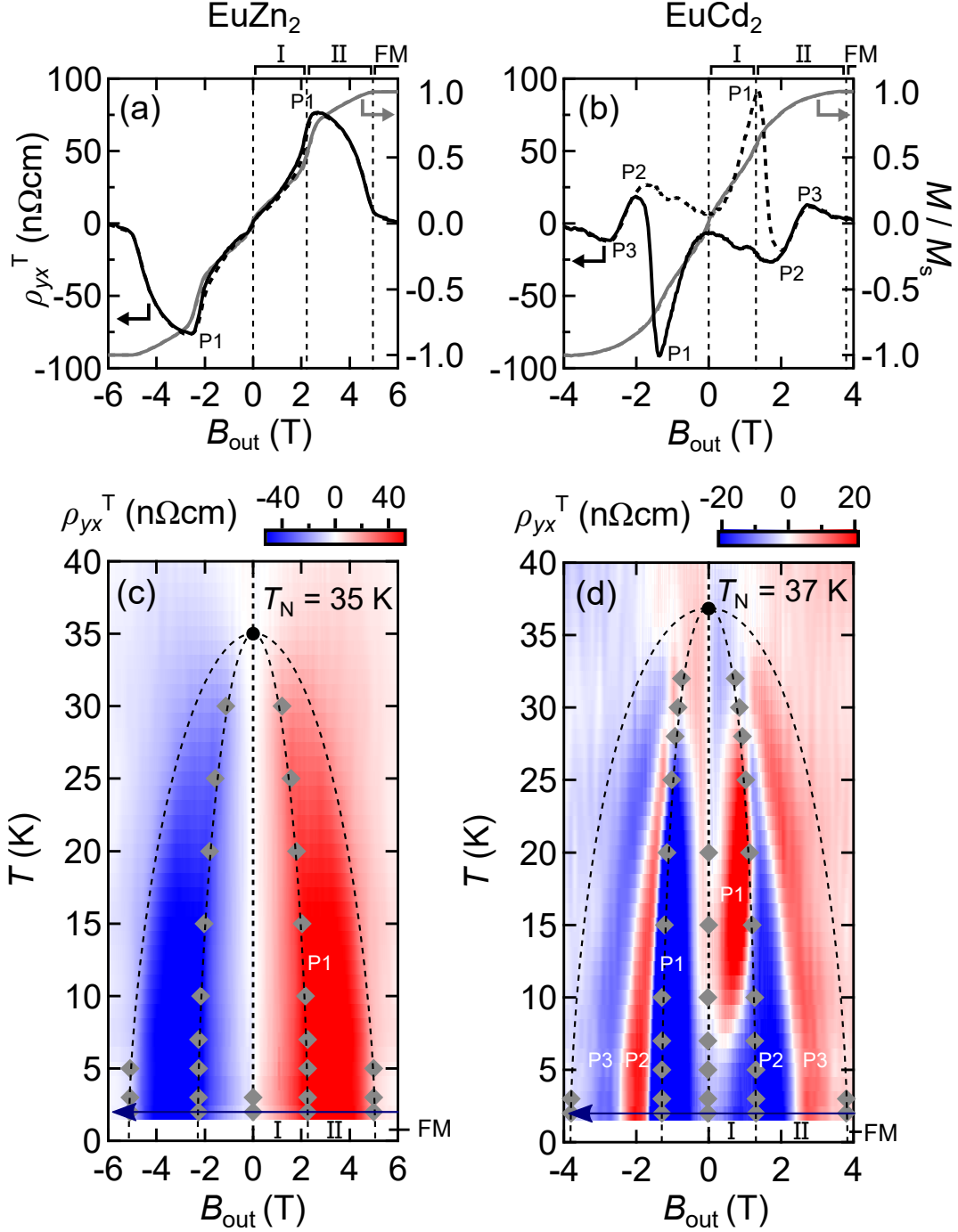


FIG. 4. Comparison of the topological Hall effect observed in EuZn₂ and EuCd₂. Topological Hall resistivity ρ_{yx}^T plotted together with the magnetization M for (a) EuZn₂ and (b) EuCd₂ films at 2 K. A solid (dashed) curve represents the data taken upon decreasing (increasing) the field from +7 (-7) T to -7 (+7) T. Mapping of ρ_{yx}^T on the B_{out} - T phase diagram for (c) EuZn₂ and (d) EuCd₂ films. Data taken in the downward field sweep is shown on the map. Magnetic transition fields determined from dM/dB are denoted by a diamond, and magnetic phase boundaries are represented by a dashed curve for a guide to the eye.